A Molecular Dynamics Study of the Pores Formed by *Escherichia coli* OmpF Porin in a Fully Hydrated Palmitoyloleoylphosphatidylcholine Bilayer

D. P. Tieleman and H. J. C. Berendsen
BIOSON Research Institute and Laboratory of Biophysical Chemistry, University of Groningen, 9747 AG Groningen, The Netherlands

ABSTRACT In this paper we study the properties of pores formed by OmpF porin from *Escherichia coli*, based on a molecular dynamics simulation of the OmpF trimer, 318 palmitoyl-oleoyl-phosphatidylethanolamine lipids, 27 Na^+ ions, and 12,992 water molecules. After equilibration and a nanosecond production run, the OmpF trimer exhibits a C-α root mean square deviation from the crystal structure of 0.23 nm and a stable secondary structure. No evidence is found for large-scale motions of the L3 loop. We investigate the pore dimensions, conductance, and the properties of water inside the pore. This water forms a complicated pattern, even when averaged over 1 ns of simulation time. Around the pore constriction zone the water dipoles are highly structured in the plane of the membrane, oriented by the strong transversal electric field. In addition, there is a net orientation along the pore axis pointing from the extracellular to the intracellular side of the bilayer. The diffusion coefficients of water inside the pore are greatly reduced compared to bulk. We compare our results to results from model pores (Breed et al., 1996. *Biophys. J.* 70:1643–1661; Sansom et al. 1997. *Biophys. J.* 73:2404–2415) and discuss implications for further theoretical work.

INTRODUCTION

The outer membrane of Gram-negative bacteria like *Escherichia coli* contains large amounts of general diffusion pores that act as molecular sieves. These porins are water-filled channels that are permeable to hydrophilic molecules with a molecular weight below ~1000 atomic mass units and may exhibit ion specificity or specificity for certain molecules like linear maltooligosaccharides, and voltage gating properties. A vast body of experimental data is available on different porins (for reviews see Jap and Walian, 1990; Schulz, 1996). In the last 5 years, many high-resolution structures of porins have been solved, including porins from *R. capsulatus* (Weiss and Schulz, 1992) and *Rhp. blastica* (Kreusch and Schulz, 1994); LamB, OmpF, and PhoE from *E. coli* (Schirmer et al., 1995; Cowan et al., 1992; Cowan, 1993); and maltoporin from *S. typhimurium* (Meyer et al., 1997); as well as the structures of some mutants. They form an important class of proteins because their location on the outside of pathogenic bacteria makes them a potential target for drugs.

Most porins share a topology that consists predominantly of β-sheets, arranged in a barrel that is imbedded in the membrane. In this paper we study one of them, OmpF, using molecular dynamics simulations. There is a large amount of experimental biochemical data on OmpF. Crystal structures of the wild type (Cowan et al., 1992) (2.4-Å resolution) and several mutants are available, including a mutant with a different structure of the constriction zone of the porin (3.0-Å resolution) (Jeanteur et al., 1994). Although for molecular dynamics studies with the currently available computational power the OmpF trimer is somewhat big, it presents an attractive model system for a larger membrane protein because of its high-resolution structure and simplicity. In addition, it forms an attractive model system for the study of transmembrane channels. Such channels play a role in biologically important processes involving excitable cells (Hille, 1992), ion transport, and transport of small molecules. Many toxins and bacteriocins also form ion channels. Clearly, there are large differences between these classes of channels, but it can be expected that there are many similarities as well, if only in the methods used to study them.

The dynamics of the porin itself is of interest in its own right. Several attempts have been made to study the dynamics of porin proteins by the use of molecular dynamics and simulated annealing in vacuum. Björkstén et al. searched for flexible zones near the constriction zone of porin from *Rhodobacter capsulatus*, using simulated annealing on a monomer, without explicit solvent or bilayer (Björkstén et al., 1994). This yielded many structures, but they found it was difficult to distinguish between physically reasonable and physically impossible states. No path was found between the structures generated. In a sequel to this work, the assumption that pore closure depends on electrostatic screening was tested (Soares et al., 1995). When the electrostatic interactions inside the constriction zone were scaled, motion of part of the L3 loop reduced the pore size considerably and reversibly. At higher temperatures, the pore also closed because of conformational changes in the L3 loop, but this change was not reversible in the time of the simulation. These results suggest that the L3 loop may play a role in voltage gating, but given the importance of elec-

Received for publication 26 November 1997 and in final form 12 March 1998.

Address reprint requests to Dr. Peter Tieleman, Department of Biophysical Chemistry, University of Groningen, Nijenborgh 4, 9747 AG Groningen, the Netherlands. Tel.: 31-503634338; Fax: 31-503634800; E-mail: tieleman@chem.rug.nl.

0006-3495/98/06/2786/16 $2.00

trostatic interactions, the absence of solvent is a significant simplification.

Watanabe et al. (1997) studied the effects position restraints on parts of the protein have on the dynamics of the porin. This is an important topic, because it seems likely that in many cases the lipid-protein interactions are not specific and merely provide a suitable environment with hydrophilic and hydrophobic zones for the membrane protein. In some cases it may therefore be possible without significant loss of accuracy to replace the membrane by much cheaper constraints. Watanabe et al. performed simulations of an OmpF monomer, using the symmetry of the trimer to effectively simulate a trimer. They found that the strength of the restraints significantly influences the dynamics of the protein, but with weak restraints the fluctuations are similar to those in the crystal. The L3 loop undergoes a displacement away from the crystal structure, closing the pore. This is caused by a breakdown of a hydrogen bond network, which they considered likely to be caused by the absence of solvent.

It will be interesting to see how these studies compare to a full simulation of a trimer. In particular, the behavior of the solvent inside the pore and the motions of the L3 loop are of interest. The structural integrity of the pore at the constriction zone, around the infamous L3 loop, is likely to depend on the presence of water as much as on anything else, because of the highly polar interior of the pore. We will investigate the structure and dynamics of this L3 loop below.

The most important feature of a general diffusion pore is the presence of a broad water-filled channel. The behavior of water inside this pore is likely to be quite different from bulk behavior, because of the strong electric field, the numerous opportunities to form hydrogen bonds with the pore lining, and the restricted area. We will investigate the behavior of water inside the pores. Comparing the results from this detailed simulation to calculations on simplified models of pores will help pinpoint the effect of some of the assumptions made in these simplified models and, it is hoped, will lead to an improved understanding of the general behavior of channel proteins.

On the methodological side of membrane protein simulations, it is useful to know what the best (or at least a satisfactory) method is for creating a starting structure for this type of system. We describe in some detail the procedure we used and discuss other methods from the literature.

Analysis of the properties of the lipids and solvent in this system and of the lipid-protein interactions will be described in a separate paper. There already are several studies of transmembrane helices and gramicidin A available in the literature (Woolf and Roux, 1996; Roux and Woolf, 1996; Shen et al., 1997; Woolf, 1997), as well as a study of bacteriorhodopsin in a bilayer (Edholm et al., 1995). However, the long simulation of the very large porin system described here should give interesting data on lipid-protein interactions, which play an important role in theoretical models for lipid-protein behavior (Mouritsen and Bloom, 1993; Mouritsen et al., 1995).

THE SIMULATION

The starting structure

The system we study here has a somewhat complicated history. The first choice to make is which lipid to use for the bilayer. Dipalmitoylphosphatidylcholine (DPPC) is a well-known lipid, both in simulations and experimentally, but its phase transition temperature is rather high, and PC lipids do not occur in the outer membrane of *E. coli*, from which OmpF is taken. The main components of the natural membrane in which OmpF is found are lipopolysaccharide (LPS) in the outer leaflet of the membrane and 16–18:1 PE lipids in its inner leaflet (Neidhardt et al., 1987). Because of its size and complexity, LPS is less suited for use in a model system, although simulations of pure LPS are feasible (Obst et al., 1997). Palmitoyloleoylphosphatidylcholine (POPE) is a good approximation for the main component of the inner leaflet of the bacterial outer membrane and has been used in functional studies of OmpF in model systems. Therefore, we decided to use this lipid. Experimental evidence suggests that LPS may play an important role in the process of insertion of the trimer into the membrane, but once insertion has taken place, the measured activities of the porin channel do not depend on the presence of LPS (Wiese et al., 1994).

To generate an equilibrated bilayer that is large enough to contain a protein the size of OmpF, we started with a POPE bilayer of 64 lipids in each leaflet, generated from randomly oriented lipids. After solvation of the lipids and 1000 ps of simulation, the structure was multiplied, using the periodic boundary conditions, to a bilayer with 256 lipids in each leaflet and simulated for a further 100 ps to remove periodicity effects. The resulting bilayer, with 512 lipids and a size of approximately $11 \times 11 \times 7$ nm, was big enough to include the protein.

As the starting structure for the porin we used the crystal structure of an OmpF mutant (Jeanteur et al., 1994). From this structure we generated a trimer using the rotation matrices in the pdb file. Placing a protein inside a bilayer in a simulation is not trivial, and in the literature different methods have been used. One method consists of simply removing enough lipids to fit the protein in the remaining hole and simulating long enough until the lipid density around the protein becomes normal. The problem with this approach is that the highly disordered lipids make it difficult to form a smooth hole, and it can take a long time for the local density to return to its equilibrium value. Woolf and Roux (1996) used a more subtle approach. They added lipids from a library of equilibrated structures to a gramicidin structure and used a rigid-body conformational search technique to remove as many bad contacts as possible. Although this method should work for larger proteins as well, it becomes more complicated in the case of a protein as large as a porin, and it has the disadvantage that the large patches of pure

lipids in the current system cannot easily be taken from a preequilibrated bilayer. Recently Shen et al. (1997) used a combination of removing a few lipids and a weak cylindrical repulsive force to clear a cylindrical area for an ideal α-helix. This seems an excellent method for molecules with a nice symmetrical geometry, but is less simple for large and rather irregular membrane proteins.

We tried two slightly different approaches. In the first attempt, a rectangular grid was placed on both the bilayer and the lipids. All lipids with atoms in grid cells that contained protein atoms were removed. This method yields a structure that can be easily energy minimized, because no overlap exists at all between the lipids and protein, but has the disadvantage that a large gap arose between the lipid and protein. The second approach used the same method, but now some overlap was allowed. This makes it impossible to energy-minimize the structure after the first step of removing lipids. However, in a series of minimization attempts followed by inspection of the resulting forces and manual removal of lipids that are in impossible positions, a starting structure was obtained with minimal disruption of the lipid bilayer.

A second problem is where to position the protein in the bilayer. In the case of OmpF it is fairly obvious what the most logical choice is; the protein is surrounded by a broad band of hydrophobic residues that is delimited by aromatic residues on both sides (Cowan et al., 1992). If the middle of this band is placed in the middle of the bilayer, the position of the end of the band in both leaflets of the membrane corresponds roughly with the acyl/headgroup interface. In this position the large loops on the extracellular side protrude into the water, whereas the short loops on the intracellular side remain mostly at the surface of the membrane (Fig. 1).

The resulting system was energy minimized, and water was added from a preequilibrated box. Water was removed from the lipid phase between the average carbonyl positions in opposing leaflets. The water molecules were allowed to relax for 25 ps around the position-restrained lipid and protein. Thirty-nine water molecules were replaced by sodium ions at positions with the lowest Coulomb potential, and the system was run for another 25 ps with only position restraints on the protein. Subsequently, an unrestrained run was carried out for 300 ps. A movie of an animation of this simulation was presented at the IUPAB conference in Amsterdam in 1996, but no further work was done on this system (Tieleman et al., 1996).

The system we describe in this paper has been derived from the system we described above by mutating residue 119 back to a glycine to obtain the crystal structure of the wild type (Cowan et al., 1992). This is a reasonable approach because the difference in structure, even around residue 119, is minimal (see Fig. 5, *green and blue lines*). The main advantage of using the older structure is that the lipids have had 300 ps to adjust to the proteins. The lipid-protein interactions are not disturbed at all by this local mutation inside the pore.

The ionization state of some residues was changed to be in agreement with continuum electrostatics calculations, according to which some amino acids have unusual ionization states due to a lack of water molecules in their environment (Karshikoff et al., 1994). We rounded the charges from Karshikoff et al. to $+1$ or -1 e and reduced the number of sodium ions to 27. The resulting structure was energy-minimized and run with position restraints on the protein for 100 ps, then without position restraints for another 100 ps. Finally, the production run of 1020 ps, without any restraints on the porin, was used for analysis. As always with molecular dynamics simulations, it does not matter how the starting structure is created, as long as the resulting starting structure is physically reasonable.

To summarize, the final structure consisted of three OmpF monomers (1,020 residues, 10,359 atoms), 318 POPE lipids (16,536 atoms), 12,992 water molecules, and 27 sodium ions, or 65,898 atoms in total. In Fig. 1 the resulting structure is shown (after 1,020 ps), with the main features of the system highlighted.

Simulation details

Two recent reviews discuss a number of technical choices to be made in bilayer simulations (Tobias et al., 1997; Tieleman et al., 1997). We made the following choices.

Most of the lipid parameters were the same as in set E in Tieleman and Berendsen (1996). The parameters for the double bond in the oleoyl tail and the partial charges on the ethanolamine headgroup were taken from the GROMOS force field (van Gunsteren et al., 1996). The lipid parameters used here have the known drawback that the density of the lipids is somewhat too high and the area per lipid somewhat too low for DPPC, which is likely to be caused by the hydrocarbon Lennard-Jones parameters (Tieleman and Berendsen, 1996; Berger et al., 1997). However, because the structure and dynamics of a DPPC bilayer, when almost the same parameter set is used, agree with most experimental data, the use of this set is not unreasonable. In addition, the set is consistent with the GROMOS force field for proteins, which is important in this mixed system. For the protein the standard GROMOS force field was used, with a modified CH_n-Ow interaction and hydrogens on the aromatic side chains (van der Spoel et al., 1996b). The simple point charge (SPC) model was used to model water (Berendsen et al., 1981). Its main advantage is that it correctly reproduces thermodynamic properties in mixed systems. Its main drawback is that the self-diffusion coefficient is too high compared to experimental data, by a factor of $\sim$1.4. However, we have shown in a previous study that this scaling factor remains approximately constant, even at the much lower diffusion rates close to the bilayer; therefore the calculated diffusion coefficients can be scaled with this factor (Tieleman and Berendsen, 1996).

A twin-range cut-off was used: 1.0 nm for the Lennard-Jones and short-range Coulomb interactions and 1.8 nm for

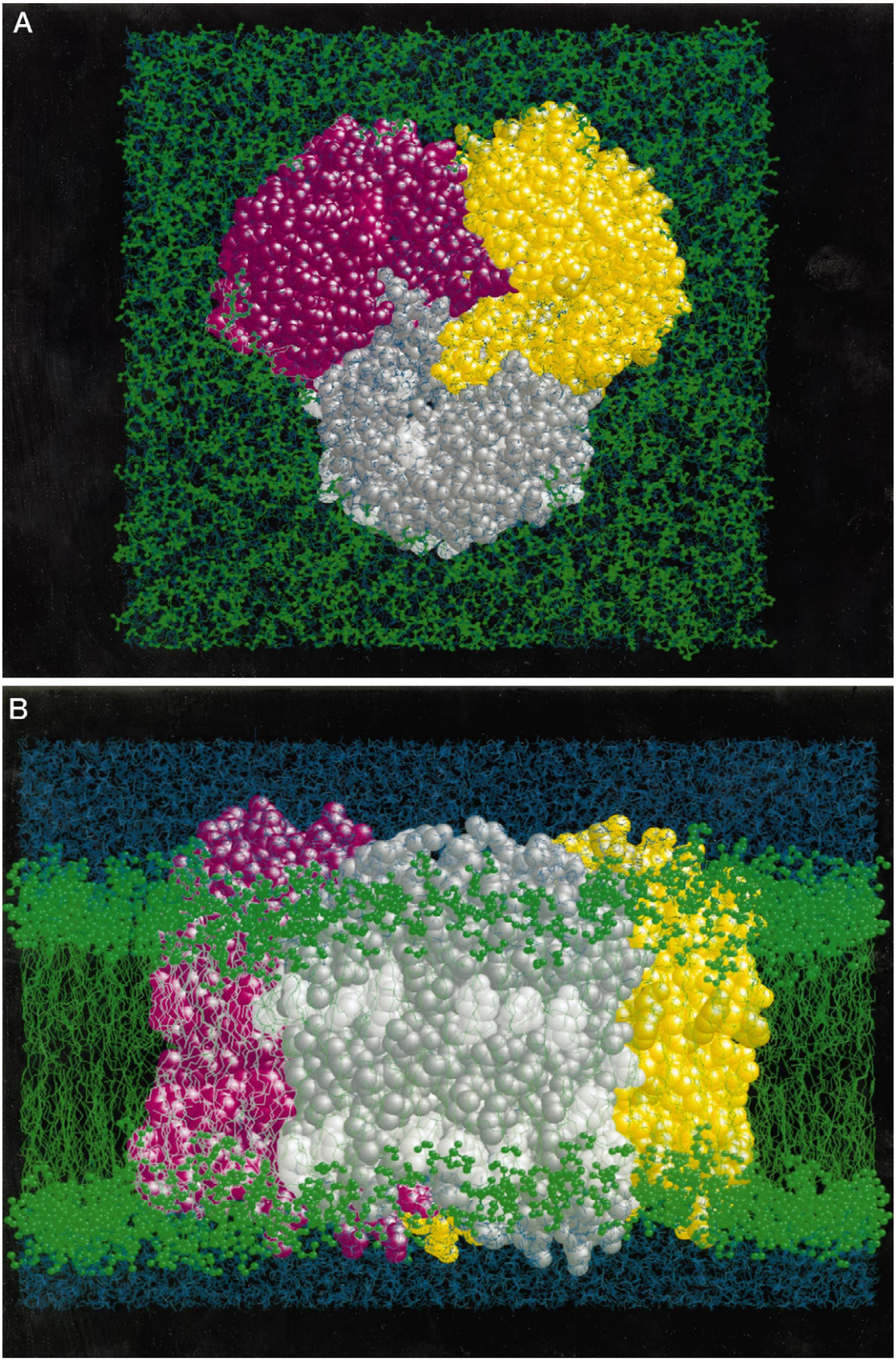

FIGURE 1 A molecular graphics view of the system. (*A*) View perpendicular to the membrane, a projection on the *xy* plane. Monomer one is colored grey, two yellow, and three magenta. Aromatic residues are highlighted. The lipid headgroups are drawn as ball and stick, the water molecules as wire frame. (*B*) Side view of the system. The intracellular side is at the bottom, the extracellular side at the top of the picture. The *z* coordinate runs from bottom to top. Water is dark blue. Obviously, atomic radii or the absence thereof are not at the right scale, but are chosen for clarity. Figures were made with RasMol 2.5 (R. Sayle).

the long-range Coulomb interactions, updated every 15 steps. Although this is not as accurate as a full treatment of the Coulomb forces using a lattice sum method, it is much cheaper (especially in a very large system like the current one) and has been tested with the force field and algorithms used in this simulation. The time step for integration of the equations of motion was 2 fs, using SHAKE to constrain the bond lengths (Ryckaert et al., 1977). The solvent, lipids, and proteins were coupled separately to a temperature bath at 310 K, using a coupling constant $\tau_T = 0.1$ ps. The system was simulated using constant pressure, 1 bar independently in all dimensions, with a coupling constant $\tau_p = 1.0$ ps (Berendsen et al., 1984). The main advantage of constant pressure in this system is that there is no good estimate of the total area of lipids plus protein. With constant pressure the area will adjust to its optimal value, given the force field parameters. In practice, the fluctuations in the area during the production run were only ~1%.

All simulations were carried out with the GROMACS package (Berendsen et al., 1995; van der Spoel et al., 1996a), at a rate of 0.5 ps/h on a single SGI Powerchallenge R8000 processor. During the production run, structures were saved every 100 steps (200 fs) and used for analysis.

RESULTS

Structure and stability

Stability of the monomers and trimer

In Fig. 2 the Cα root mean square deviation (RMSD) of the trimer as a whole and the individual monomers is plotted with respect to the crystal structure. The RMSD for the trimer slowly increases, from 0.19 nm to 0.23 nm in a nanosecond. The RMSD for the individual monomers (the Cα atoms of each monomer fitted separately) is ~0.20 nm after 1 ns and only increases by 0.01 nm in the last 500 ps. In Fig. 3 the locations of the β-sheets, loops, and turns and

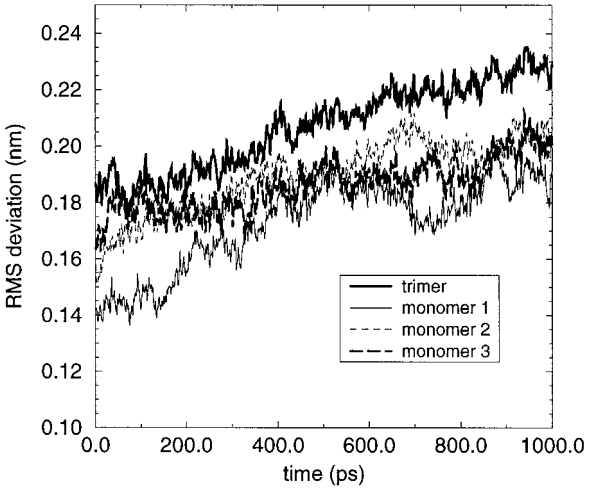

FIGURE 2 The Cα root mean square deviation of the trimer and the monomers, fitted to the crystal structure.

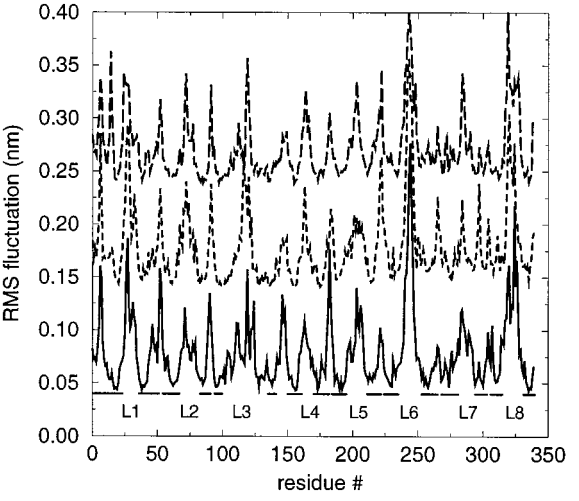

FIGURE 3 The root mean square fluctuation of the Cα atoms with respect to their average position. The three curves are on the same scale. The solid line is monomer one, the dashed line (shifted by 0.1 nm in the y direction) monomer two, the long dashed line (shifted by 0.2 nm in the y direction) monomer three. The labels indicate the positions of the loops, the bars the position of the β-sheets.

the RMS fluctuation of each residue (Cα-atoms) with respect to its average position are plotted separately for the three monomers. It is easy to recognize the important secondary structure elements in this plot: the peaks correspond to loops or turns. The largest fluctuation is found for the L6 loop, a large loop on the extracellular side that exhibits a slow "waving" motion. The β-strand residues of the barrel show a low mobility with values of 0.05 nm.

Although the pore size fluctuates heavily during the simulation (see below), this is unlikely to be caused by significant changes in the secondary structure. The secondary structure, as defined by DSSP (Kabsch and Sander, 1983), does not fluctuate much during the time of the simulation (Fig. 4; only the first monomer is given). The β-strands that form the main barrel structure remain intact. It is remarkable how stable the six-residue helix in the L5 loop (197–202) is, considering this is a solvent-exposed loop. The differences between the three monomers are small and are mostly located in the solvent-exposed loops on the extracellular side, which do not have a definite secondary structure. An example is the L6 loop (236–252), which has no appreciable structure in monomer one, but is partly β-sheet or bend for a couple of hundred picoseconds in monomers two and three. This loop also has by far the highest RMS fluctuation.

The structure of the L3 loop

The fluctuations of the α-helical structure of residues 105–112 of the L3 loop form the most interesting difference between the monomers. This small helix remains present in monomer one during the entire run. In monomer two, part of the helix assumes a 1–3 helix conformation and fluctuates between 1–3 and α-helix throughout the simulation. In monomer three, the α-helix has been distorted at the start of

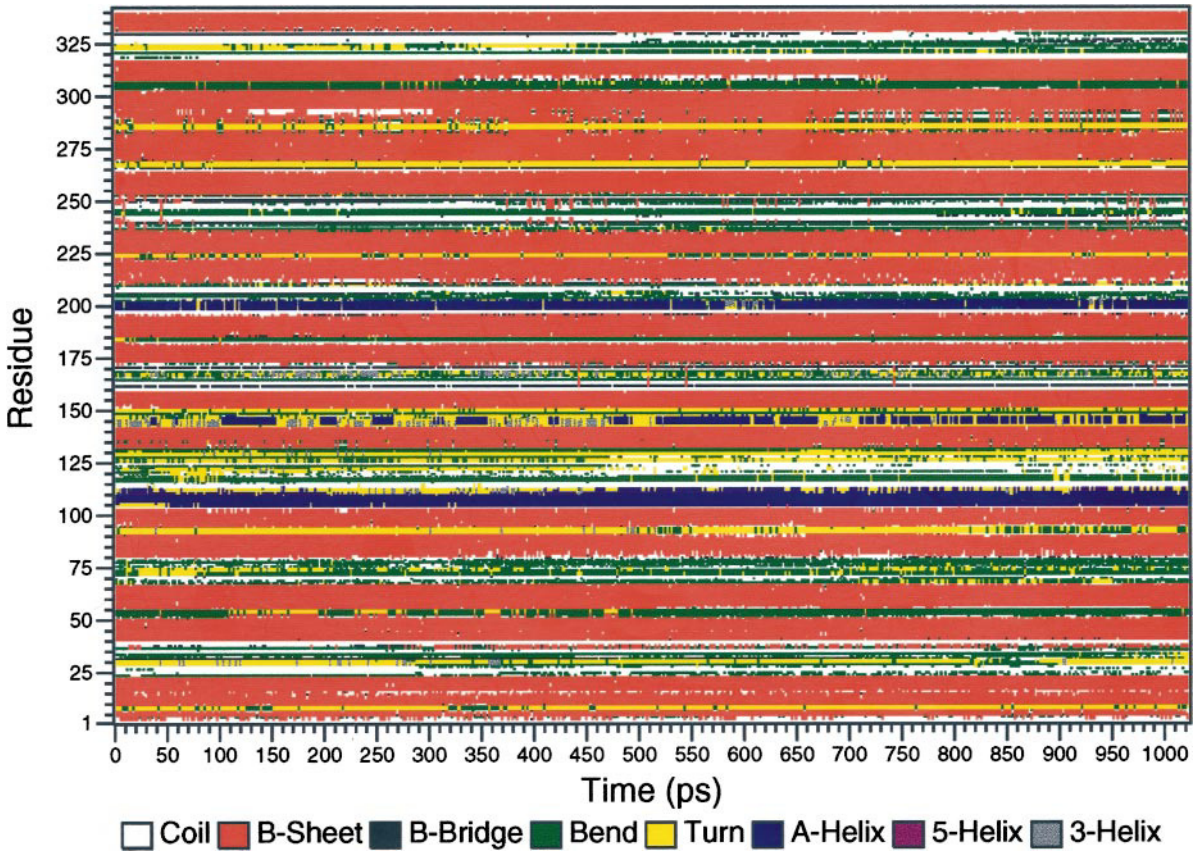

FIGURE 4 Secondary structure as function of time for the first monomer as calculated by DSSP (Kabsch and Sander, 1983).

the simulation, and the residues assume a 1–3 helical form. However, in none of the pores do we find a large motion of the backbone of the L3 loop. A projection of the L3 loop and surrounding pore, taken from a 3-nm-wide slab encompassing residues 100–150 at 0, 500, and 1000 ps in the simulation, is shown in Fig. 5. There is obviously some displacement of the backbone atoms during these 1000 ps, but both the L3-loop and the barrel walls seem stable.

The RMS fluctuation of the residues of the L3 loop has been magnified in Fig. 6. Although the mobility of this loop, based on Fig. 3, is not especially large compared to other loops and turns, it is interesting to see that the most flexible residues are near Gly^{119}. In the crystal structure this residue fits into the wall of the pore, but in the mutant, where it has been replaced by the larger and charged Asp, it protrudes into the pore opening, effectively dividing the pore in two and greatly reducing the size of the pore (Jeanteur et al., 1994).

In Fig. 7 a detailed stereo picture of the pore constriction zone of monomer one at the end of the simulation is shown, with important residues highlighted. Arg^{42}, Arg^{82}, and Arg^{132} form a positively charged cluster of basic residues on one end of the pore. Arg^{82} is not charged in the simulation; it experiences a huge shift in pKa in the calculations of Karshikoff et al. Above these arginines, Lys^{80} is another positively charged residue. On the opposite side of the pore, Glu^{117} and Asp^{113} are negatively charged, contributing to the strong transversal field. Asp^{121} is not charged.

Also shown are a number of acidic residues that are uncharged because they are shielded from solvent. This is the case for Asp^{312} and Glu^{296}, which form a hydrogen bond network with Ser^{272}. Asp^{127} forms a hydrogen bond with the backbone oxygen of Ala^{237} in the crystal structure, but this bond is not present in the structure after the simulation. Overall, the orientation of the key basic and acidic residues is not much different from the crystal structure (compare Figure 2 *A* in Karshikoff et al., 1994).

Pore properties

Pore radius profiles

To analyze the size of the pore opening, we used the program HOLE (Smart et al., 1997). HOLE calculates the radius of a pore at a given distance along the pore axis by determining the maximum size for a spherical probe (using a Monte Carlo search algorithm) that will fit in the pore without overlap with the van der Waals radii of any of the atoms that line the pore. The program needs the coordinates of a point inside the pore, the approximate direction of the channel axis, a set of atomic coordinates, and a set of atomic radii. This method has been applied to several channel-

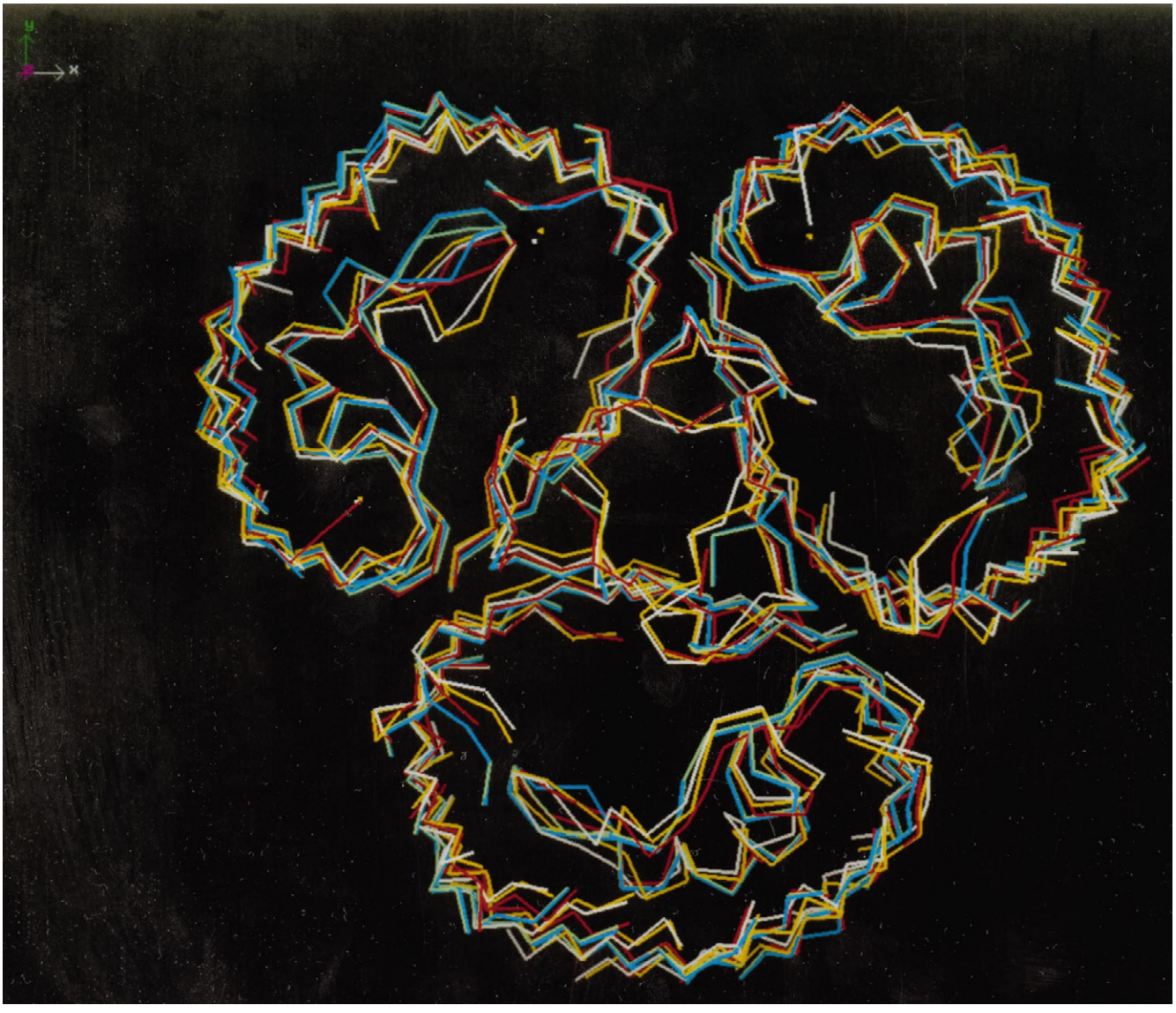

FIGURE 5 A superposition of the protein backbone in a 3.0-nm-thick slab containing the L3 loop. Green is the crystal structure of the wild type, blue the crystal structure of the mutant, red the structure at $t = 0$ ps, yellow at $t = 500$ ps, and white at $t = 1000$ ps. Figure made with Quanta 97 (Molecular Simulations).

forming proteins and helix bundle models (Smart et al., 1997; Breed et al., 1997).

To get an impression of the area of the pore as a function of the position along the pore axis, we calculated the pore radius profiles of the crystal structure (Fig. 8). From the intracellular side, the pore radius slowly decreases from over 1 nm to slightly less than 0.4 nm at its narrowest point. Going toward the extracellular side the radius rapidly increases to over 1 nm.

Also given in Fig. 8 are the pore radius profiles of the starting structure of monomer two and the average profile of each of the three monomers. At the start of the production run, the radius of the pores is already smaller than in the crystal structure. It is clear that in all three monomers, the average radius lies below the radius of the crystal structure. Although the profile for each of the monomers does not change much when different intervals during the simulation are taken, the difference between the three pores is fairly large. The most important difference is the considerably smaller minimum radius of the third monomer. A typical minimum radius is 0.25 nm.

An alternative, more indirect way to look at the size of the pore opening is by calculating the water density as function of the z coordinate. Combining this water density profile with the size of the system and assuming bulk density for water everywhere in the system, the water-filled area as a function of z can be calculated. This yields a minimum radius of 0.5 nm for a pore, roughly twice the size calculated by HOLE for the simulation structures.

One of the interesting results from the MD simulation is the behavior of the pore as a function of time. The crystal structure shows only one conformation, but obviously ther-

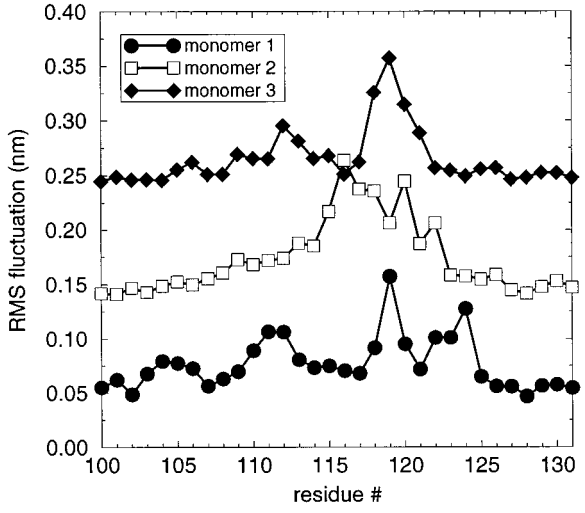

FIGURE 6 The root mean square fluctuation of the Cα atoms of the L3 loop with respect to their average position. The three graphs are on the same scale, but the upper two have been shifted by 0.1 and 0.2 nm, respectively, in the positive y direction.

mal motion will change the size and shape of the pore in time. Because the conductance properties of the pore are mostly determined by the narrowest regions, the fluctuation of the minimum radius is a interesting property to look at.

In Fig. 9 the minimum radius of the pore as a function of time has been plotted. Monomer three has a considerably lower minimum radius than monomers one and two, with a minimum value of close to 0.1 nm. The average radius is 0.16 nm, and the maximum radius 0.2 nm. This is much smaller than the 0.35 nm of the crystal structure. The difference between the other two monomers is less, with a minimum radius of 0.18 nm and 0.16 nm, respectively, an average radius of 0.25 nm and 0.24 nm, and maximum radii of 0.33 nm and 0.29 nm. The spread around the average values is high, and over a nanosecond the minimum area of the pore varies rapidly. The maximum value of 0.33 nm for monomer one is close to the value of 0.35 nm for the crystal structure. This value occurs after 600 ps of production run, showing that there is no trend toward closing of the pores. Fig. 9 as a whole leads to the same conclusion: at least for monomers one and two, the pore size toward the end of the simulation is about the average value, and there does not appear to be a trend toward closure. It is somewhat less clear for monomer three, but in that case as well, there is no obvious trend toward closure of the pore.

Conductance calculations

Pore radius profiles $r(z)$ can be related to a conductance using

$$G_{\text{upper}} = \left[\int_a^b \frac{\rho}{\pi r^2} \, dz \right]^{-1} \tag{1}$$

where the pore runs from a to b, and the pore is assumed to be filled with an electrolyte with bulk resistivity ρ. Following Smart et al., we used $\rho = 0.08\ \Omega$m for 1 M KCl (Smart et al., 1997). The calculated conductance overestimates the real conductance (hence G_{upper}), because in this simple model bulk properties for the electrolyte are assumed. In reality, both the local ion and water diffusion coefficients inside the pore are lower than in bulk solution, for various reasons. To a first approximation, these combined effects can be summarized in an empirical correction factor s with which to scale the calculated conductance. For porin, Small et al. determined a value of $s = 5$—thus the experimental $G_{\text{exp}} = G_{\text{upper}}/s$. The experimental conductance of OmpF in 1 M KCl is 700 pS, and this value is reproduced by a HOLE radius profile of the OmpF crystal structure, using $s = 5$ (Smart et al., 1997).

In Fig. 10 the calculated G_{exp} has been plotted. The points at which the pore has a radius of 1.4 nm were taken as upper and lower limits along the pore axis, corresponding to z coordinates of 0.2–0.4 nm at the intracellular side and 6.0–6.5 nm at the extracellular side. The precise value does not matter much, because the contribution to the total conductance of the widest part of the pore is small. Monomer three has the lowest conductance, by a factor of almost 1.5, compared to the other two. Each of the three profiles fluctuates considerably; the average conductances (SD) are 333 (27) pS, 299 (29) pS, and 204 (28) pS, or less than half the value for the crystal structure. The minimum and maximum values differ by a factor of almost 2 in pores two and three, and by somewhat less in pore one. These calculations are extremely sensitive to the area calculations. From comparing Figs. 9 and 10 it is clear there is a strong correlation between the minimum radius and the calculated conductance. If the radius profile for pore one is multiplied by 1.2 (which is comparable to what one might get when, instead of a spherical probe in HOLE, a spherocylindrical probe is used), the conductance for pore one becomes 480 (40) pS, or a 50% increase.

Water properties

Diffusion

We calculated the translational diffusion coefficient from the mean square displacement using

$$\lim_{t\to\infty} \langle (\mathbf{r}(t) - \mathbf{r}(0))^2 \rangle = 6Dt \tag{2}$$

with similar equations for the x, y, and z components. A water molecule was assigned to a slice of 0.12-nm thickness based on its position at the start of an interval of 5 ps, the last four of which were used to calculate the mean square displacement. The calculated diffusion coefficients were then averaged over the entire slice.

The results are given in Fig. 11. The profiles for diffusion in the x and y directions are almost the same, which can be expected because of the trimer's rotational symmetry. In the

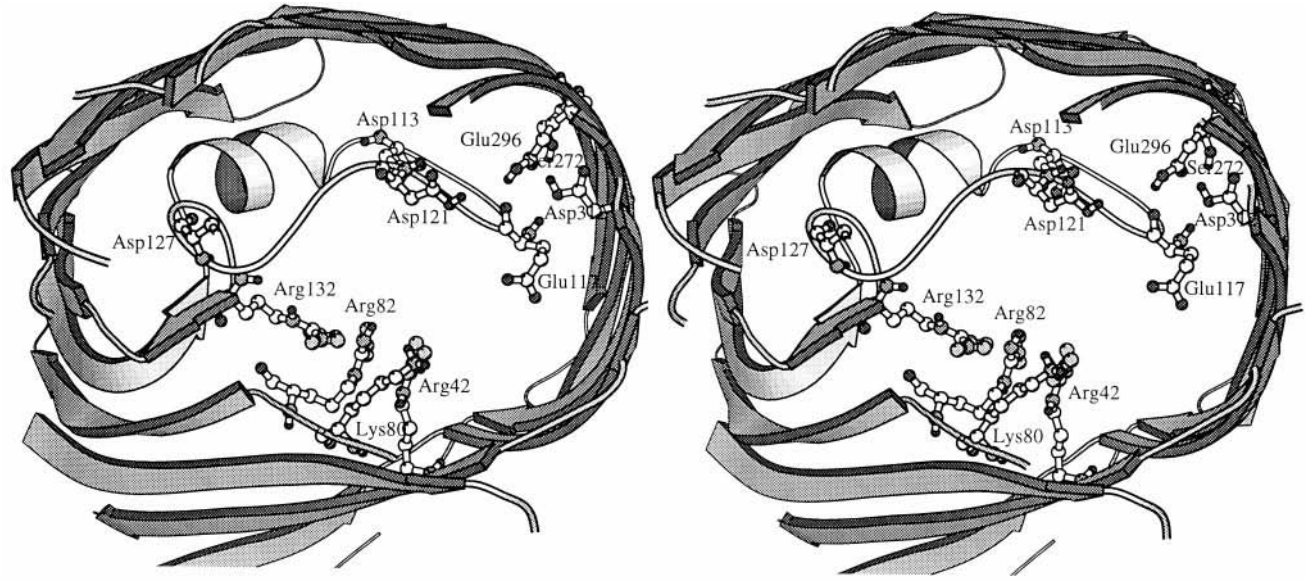

FIGURE 7 Stereo view of the constriction zone of monomer one, after 1020 ps. Key residues inside the pore are highlighted. Figure made with Molscript (Kraulis, 1991).

water layer the diffusion coefficient is close to the value for bulk SPC at 310 K, 5.1×10^{-5} cm^2 s^{-1}. In the vicinity of the bilayer, D_z decreases faster than D_{xy} because motion toward the lipid bilayer is restricted. Inside the porins D_z becomes higher than D_{xy}. There is a small peak at the intracellular side, indicating that water diffuses more freely locally in that wide part of the pore than in the lipid headgroup zone. The diffusion coefficients in the narrowest part of the pores are almost an order of magnitude lower than their bulk values.

Water structure inside the pores

In Fig. 12 the average dipole component of water molecules with respect to the normal (z axis) to the bilayer is plotted. The maximum magnitude in the z direction is 16% of the dipole moment of a SPC molecule, 2.274 Debye (Berendsen et al., 1987).

Near the bilayer the water dipole points toward the lipid phase. The x and y components are much smaller, and reach appreciable values only inside the bilayer (in the pores). The orientation of water molecules with respect to the bilayer inside the poor varies strongly with the position in the pore; the maximum degree of orientation is comparable to the orientation caused by the lipid headgroups, ~15% of the maximum dipole. At the intracellular side, close to the constriction zone, there is a strong peak in the graph; the water dipoles point toward the intracellular side. In the zone between 3 and 4 nm, there is no preferential orientation along the axis. In this part, water molecules feel the strong transversal field near the constriction zone and are strongly

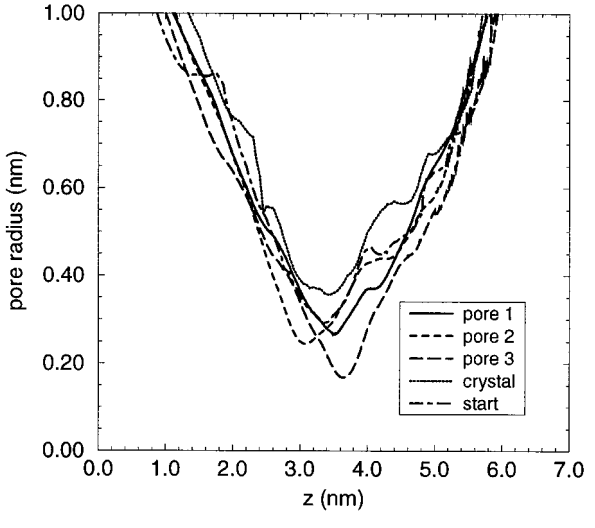

FIGURE 8 Pore radius profiles. *Pore 1, pore 2, pore 3* are averages over 1 ns. *Crystal* is the pore radius profile of the crystal structure, and *start* is the pore radius profile of monomer two at the start of the production run.

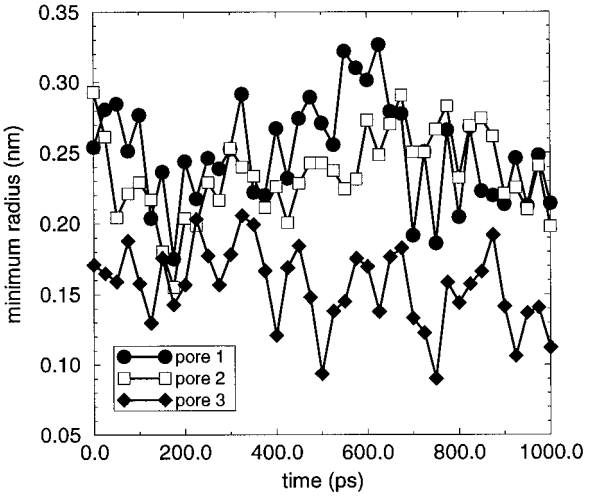

FIGURE 9 The minimum radius of the pores as a function of time.

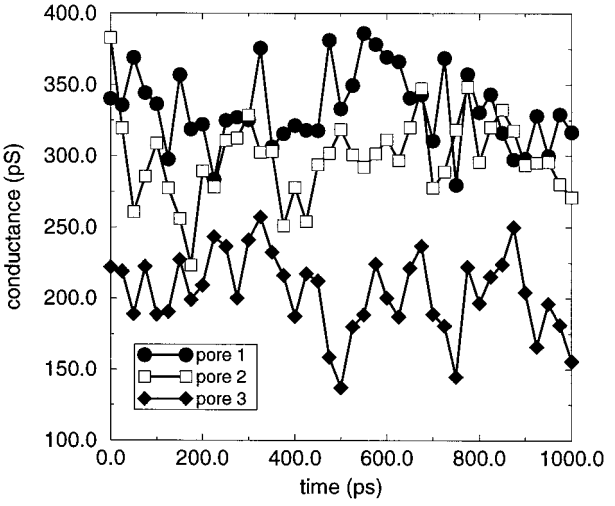

FIGURE 10 The predicted conductance for 1 M KCl of each of the three monomers.

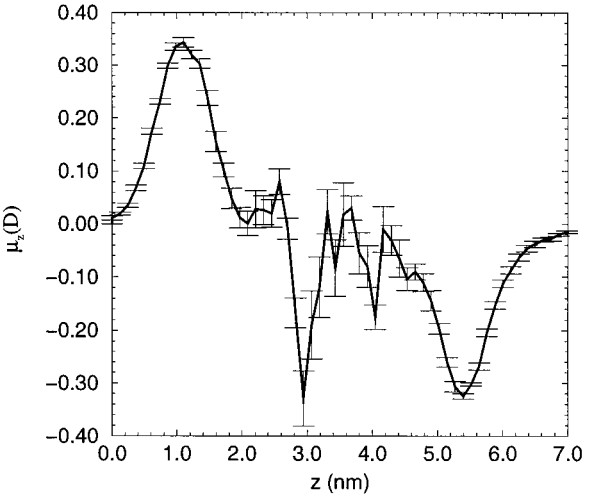

FIGURE 12 The z components of the average water dipole moment. If there is no preferential orientation, the orientation would be zero everywhere; if the water molecules are fully aligned along an axis, μ_{axis} would be the total dipole moment of SPC, 2.27 Debye.

ordered perpendicular to the pore axis. Beyond the constriction zone, at 4 nm, there is another, lower peak in the orientation. Water dipoles also point toward the intracellular side. Moving out of the pore, and out of the influence of the protein, the lipids take over and the water orientation is the same as on the intracellular side: water molecules pointing on average toward the bilayer. Because the orientation of the water dipoles with respect to the z axis is taken, the z components of the water dipoles are negative on the extracellular side of the membrane.

A more detailed picture of the orientation of water molecules in the system can be obtained by calculating the average dipole moment $\langle\mu\rangle$ per water molecule on a rectangular grid. This $\langle\mu\rangle$ is related to the polarization P by $P = \langle\mu\rangle/v_w$, where v_w is the volume of a water molecule. P, in turn, is related to the total electrostatic field at a given point by a Langevin function,

$$P(E) = \frac{\mu_0}{v_w}(\coth(x) - 1/x) \tag{3}$$

where $x = \mu E/k_B T$, where μ_0 is the dipole moment of one water molecule, and v_w is its volume. Average dipole moments of 0.5, 1.0, 1.5, and 2.0 Debye correspond to field strengths of 0.4, 0.9, 1.6, and 4.7 V/nm, respectively.

These data are hard to visualize in three dimensions; instead, we use a number of projections on the xy plane at positions along the pore axis with a separation of 0.36 nm (Fig. 13). The scale of the vectors is in 0.1 e nm, or alternatively, an arrow with a length of one grid cell corresponds to 1.3 Debye. Recall that the total dipole moment of one SPC molecule is 2.27 Debye. The projections run from the intracellular to the extracellular side of the pore.

The first projection gives the water orientation in a plane just behind the lipid headgroups. The largest arrows are water molecules that are hydrogen bonded to (partially) charged atoms in the pore walls or in the short loops on the intracellular side of the protein. The dipole moment of water not bound to the pore walls is considerably smaller. However, even relatively far from the constriction zone, a somewhat circular pattern can be seen.

Closer to the center of the membrane, most of the water molecules outside the pore have disappeared. The pores have become narrower and the dipole magnitudes inside the pore have increased somewhat. Around 2.5 nm, still 0.5–1.0 nm below the constriction zone, an appreciable orientation along the pore axis begins (Fig. 12). The sixth and seventh slices are close to the constriction zone. All water molecules in this part of the pores have high average dipole moments, with most of them around 1.3 Debye, or over half the total dipole moment of one water molecule. There are several

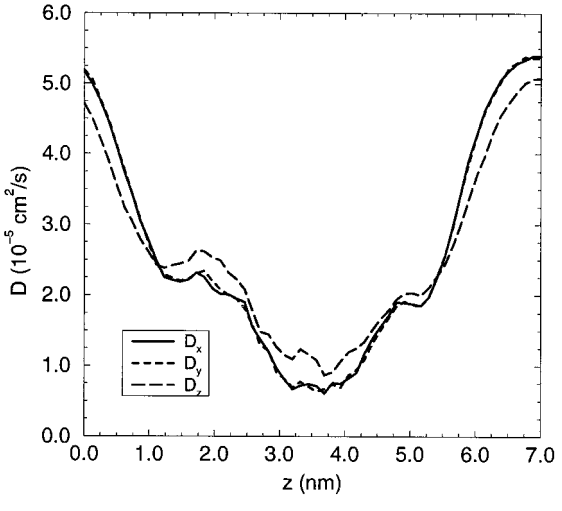

FIGURE 11 The translational diffusion coefficients D_x, D_y, D_z as a function of the distance along the channel axis, averaged over the trimer. The bulk value for SPC at 310 K is 5.1×10^{-5} cm^2 s^{-1}.

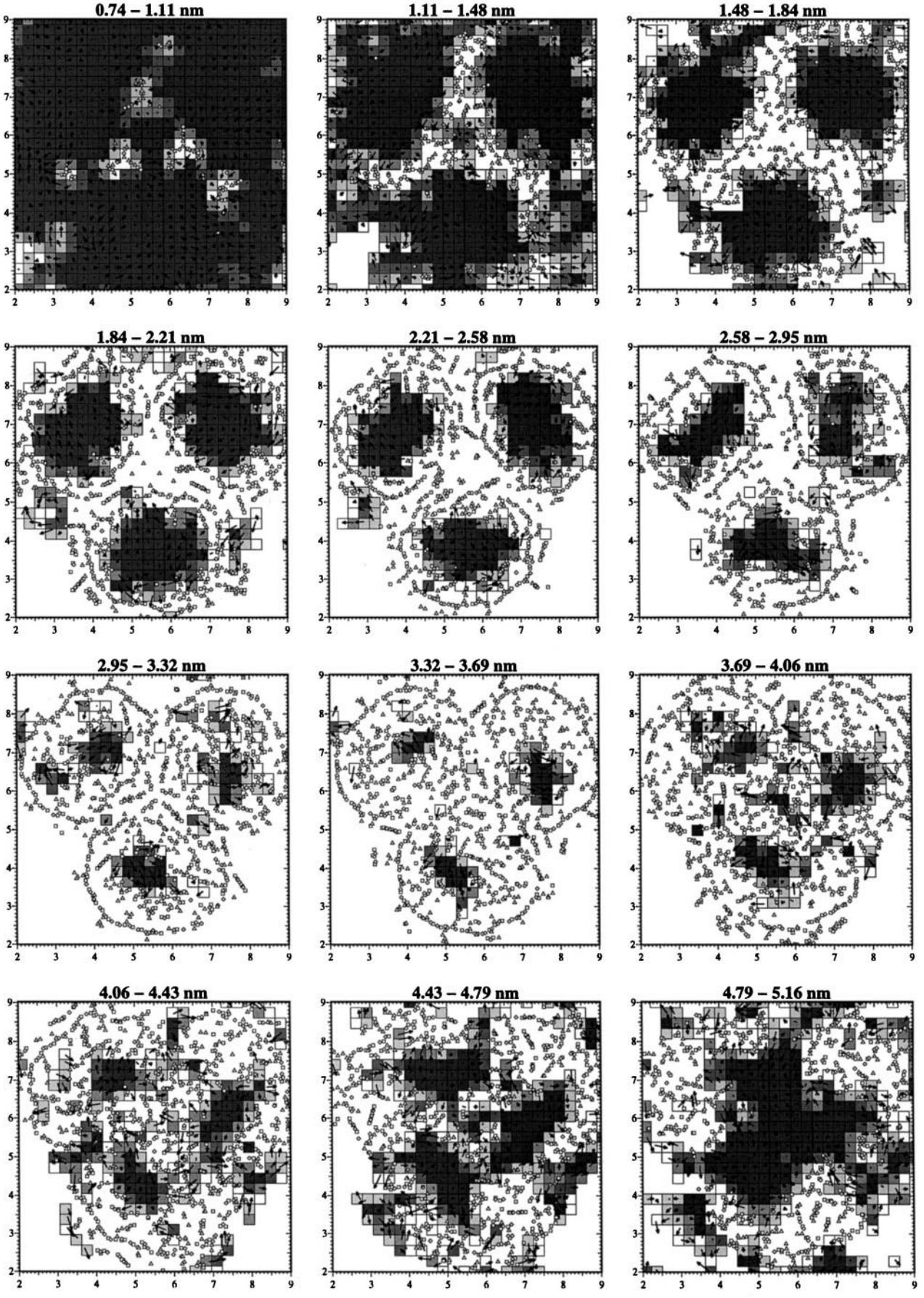
0.74 – 1.11 nm
1.11 – 1.48 nm
1.48 – 1.84 nm
1.84 – 2.21 nm
2.21 – 2.58 nm
2.58 – 2.95 nm
2.95 – 3.32 nm
3.32 – 3.69 nm
3.69 – 4.06 nm
4.06 – 4.43 nm
4.43 – 4.79 nm
4.79 – 5.16 nm

water molecules outside the pore itself; many of these have dipoles of ~2 Debye, indicating highly directed water molecules hydrogen bonded to protein atoms. As in the first figures, the patterns for the three monomers are very similar.

Between 3.3 and 3.7 nm, the narrowest point of the pores is found. Monomer three (upper left one in the graph) clearly has a smaller area than the other two, and there is a large difference in water orientation between this slice and the previous slice.

In the eighth slice we have passed the constriction zone and are moving toward the extracellular side. Water has penetrated along the symmetry axis and is hydrogen bonded to protein atoms in the center of the trimer. The water order patterns are somewhat chaotic, but the strongest ordering is observed for atoms lining the porin walls, whereas toward the center of the pores, the average dipole moment decreases.

These features become more pronounced as we move toward the outside. In the middle of the pores water loses its orientation, against the pore walls water shows a higher degree of ordering, and single water molecules or small clusters are strongly hydrogen bonded to loops and the center of the trimer.

In the last view, the middle of the bilayer has been flooded and the three channels are connected. The recognizable parts of the protein are protruding loops. Both in the protein and in the water structure, the threefold symmetry is clear.

DISCUSSION

Stability and length of the simulation

The length of a simulation is always a point to worry about. Would the results change much if we had simulated for 2 or 3 ns?

The fast motion of free or almost free water will be sufficiently sampled in 1 ns (a free water molecule diffuses over more than 5 nm in 1 ns), and the statistical uncertainty in properties like the water diffusion coefficient, density profiles, and average water dipole moments is small. Doing the same analysis over shorter parts of the trajectory does not significantly alter the results, although the results are more noisy.

The slowest motions we analyzed, although not in much detail, are those of the protein. Overall, the RMS fluctuations correlate nicely with the secondary structure in the crystal structure. The trimer and monomers as a whole remain intact during the simulation, and almost all of the flexibility is found in the loops and turns outside the β-barrel. The β-strands themselves are the least mobile parts of the protein, and their secondary structure does not change noticeably during the simulation.

We have an internal check for convergence for properties that are not collective across the trimer, because we have three monomers. Although the calculated water orientation profiles are not exactly the same for each monomer, the general picture that would be obtained from each of the monomers is the same as the picture we have described here. The only significant difference in structure is found at the L3 loop. In monomer three, there is no α-helix in this loop and there is considerable deviation from the crystal structure, narrowing the pore. The tip of the loop changes most during the simulation, but already in the starting structure of the production run, this loop is moved into the pore opening, compared to its location in the crystal structure (Fig. 5). The reason for this turns out to be that the geometrical criterion used to solvate the porin allowed water molecules to be placed between the loop and the pore wall. These water molecules appear to be trapped, and it is questionable whether they could get to that location in the real system. Upon removal of 15 water molecules around the L3 loop in monomer three, and a further 150 ps of simulation, part of the loop folds back slightly toward the wall, but the pore remains smaller than the other two pores.

The possibility of trapping water molecules in unfavorable internal positions during the initialization procedure may be a serious cause of artefacts in simulations of biological macromolecules. Whether a water molecule is placed correctly can be judged from its free energy; because particle insertion methods are inadequate for water in dense systems, it would be necessary to apply a computationally expensive thermodynamic integration over a path involving the creation or annihilation of a water molecule.

The role of the L3 loop

The L3 loop merits a closer look because of its location in the center of the pore. Residues in this loop are responsible for the strong transversal electric field and possibly for voltage gating behavior. The sequence PEFGG (116–120 in OmpF) is well conserved in a porin superfamily of 14 proteins, and determines the structure of the tip of the L3 loop (Cowan et al., 1992). As is clear from the drastic effect of the point mutation Gly → Asp on the pore properties, this is an important area (Jeanteur et al., 1994). Interestingly, the

FIGURE 13 The average orientation of water dipoles in a number of slices perpendicular to the channel axis. We used a $40 \times 40 \times 20$ grid, corresponding to grid cells with size $0.28 \times 0.27 \times 0.36$ nm. For each cell the average water density and average orientation of water molecules in that cell were calculated and plotted. If a grid cell is not drawn, the density is less than 0.1 of bulk density. Gray-scale values indicate the density in increments of 0.2, with the darkest color corresponding to the bulk density of water. The arrows start at the average position of the oxygen atom of the contributing water molecules, and the length corresponds to the magnitude of the projection of $\langle\mu\rangle$ on the xy plane. A length of one grid cell (~0.3 on the axes) corresponds to 1.3 Debye. Figure titles give the z coordinates of the slice. The average position of protein atoms is given by squares for positively charged atoms, diamonds for negatively charged atoms, and triangles for neutral atoms.

highest RMS fluctuations in the L3 loop in our simulation are found for residues around 119.

Voltage gating in porins is a somewhat controversial phenomenon. It has been observed in a number of porins, but it is unclear whether voltage gating has a biological function, because there is at most a small Donnan potential across bacterial outer membranes (Schulz, 1996). Soares et al. (1995) used simulated annealing methods to find possible pathways for the L3 loop in porin from *Rhodobacter capsulatus*, but did not find reversible paths between the structures they generated. Simulations of porins without explicit solvent should be regarded with caution, because it is difficult to distinguish between physical motion and force-field and algorithmic artefacts. Pore size or shape fluctuations caused by major motions of the L3 loop are not observed on the time scale of our simulation; the difference in structure between pore three and the other two is due to the creation of the starting structure, and even in pore three the structure of the loop does not change much during the simulation. This is in agreement with the interpretation by Cowan et al. (1992), who suggested on the basis of the crystal structure and physical intuition that it seems unlikely that the L3 loop in OmpF is mobile enough to close the pore. It is possible that such motions play a role on a much longer time scale, but the times associated with experimental measurements of gating behavior in porins are so slow that it may involve much more than a simple rearrangement of a loop (Berrier et al., 1992; Jap and Walian, 1990). It has been suggested that gating is actually caused by large cations that block the pore under the influence of a field (Schulz, 1996). An alternative explanation is offered by atomic force microscopy measurements, which suggest that the large extracellular loops may exist in a conformation in which loops fold toward the center of the trimer, closing the pore (Schabert et al., 1995). It is conceivable that L6 does this.

Pore radius and conductance calculations

The use of a spherical probe is a severe approximation in calculating the pore area; a few atoms from a side group protruding into the main pore will have a large effect on the radius of the pore calculated by a large probe. Using much smaller probes or water densities gives more information on the area not occupied by protein atoms, but this information is harder to interpret in terms of molecules permeating through the pore.

The conductance calculations themselves are simply based on the area of the pore opening. There are two main assumptions in these calculations, namely that the dielectric and hydrodynamic properties of water in the pore are the same as in bulk water, and that the mobility of ions in the pore is the same as in bulk water. Obviously, both of these assumptions are rather severe, because a wide body of evidence from simulations, as well as common physical sense, suggests that both of these properties will have much lower values in the restrictive environment of a small pore with charges lining the walls. Smart et al. suggested a simple correction to compensate for the effects of these assumptions, using experimental conductance data for OmpF and gramicidin A (Smart et al., 1997), but it is likely that the correction factor itself will depend on the pore size. Within this simplified framework, using a spherical probe makes sense. The only way to get accurate results for the transport behavior of different molecules is to use nonequilibrium molecular dynamics simulations, but these are computationally expensive.

It turns out that the crystal structure of the porin has the largest effective radius of all structures observed over the course of our simulation, although values reasonably close to those of the crystal structure are seen occasionally. It seems that the crystal structure represents the "most open" state, with the L3 loop fitted nicely in the wall of the porin barrel. Especially in the highly charged environment of the pore constriction zone, where a number of residues are likely to have uncommon ionization states, one should be cautious with MD data. However, the backbone structure of each of the monomers was quite stable during the simulation, and no indications of major force-field problems are present. The most reasonable conclusion is that the crystal structure gives an upper limit for the area of the pore, confirming the hypothesis of Cowan et al. (1992) and Cowan (1993). Watanabe et al. found that the pore opening almost completely disappeared during the 100 ps of simulation time, but they give as possible reasons for this the use of standard ionization states and, more likely, the absence of explicit solvent.

One should take into account when making conductance calculations of the simplified type we used here that considerable differences may exist between pore sizes calculated from MD simulations and from crystal structures; using empirical correction factors is therefore problematic.

Why would one bother with these approximate values? Many channels are currently being studied experimentally for which there are no structural data. Any method of linking conductance, or any other available data, to the structure of pore-forming molecules can help to make better models, pending solution of the structure by x-ray, NMR, or microscopy techniques. In a nicely symmetrical pore formed by a helix bundle, this type of calculation can make it possible to exclude certain models, which is quite useful (Breed et al., 1997).

The behavior of water inside the pores

The diffusion properties of water inside channel models differ greatly from their bulk values. Both the reorientational correlation times and the translational diffusion coefficients are reduced compared to their bulk values. Sansom et al. found translational diffusion to be between one and five times slower inside cylindrical cavities with different radii (Breed et al., 1996; Sansom et al., 1996). In more realistic pore models using polyalanine helices, polyalanine β-barrels, or amphipathic helices, a similar range was found

(Breed et al., 1996). We find a larger reduction than in the simple model pores without complicated charged lining and constriction zones, but basically confirm earlier findings on different model channels.

The dielectric behavior of water inside pores is of great interest for modeling ion channels. Computationally cheap and relatively simple continuum electrostatic calculations require accurate values for the dielectric constant in water-filled ion channels (Warshel and Åqvist, 1991). Both experimental and theoretical data suggest that water inside pores has a lower dielectric constant than bulk water, because of the reduced orientational freedom (Sansom et al., 1997). To actually calculate the local dielectric constant, one can carry out simulations at different applied field strengths and measure the polarization as a function of the field, or one can analyze the fluctuations in the polarization in an equilibrium simulation. Both methods are involved and are beyond the scope of the current work, but it would be interesting to see how estimates of the dielectric constants in the pore compare to those calculated by Sansom and co-workers for model pores at different field strengths (Sansom et al., 1997).

Intuitively, one expects in the case of OmpF that a single dielectric constant will not be sufficient to accurately describe the pore interior. Diffusion coefficients decrease by almost an order of magnitude across the pore, and the average dipole moment (degree of ordering) of water molecules strongly depends on the location in the pore. The magnitude of these dipoles of water inside the channel can be up to 2 Debye, or ~50% of the molecular dipole moment, indicating a local field of 10^9 V/m. Under these field strengths, water will not behave as a linear dielectric medium. The further away from the constriction zone, the wider the pore and the lower the average orientation of water becomes. The screwlike field that was observed by Karshikoff et al. (1994) is difficult to recognize in the water orientation plots. It is clear that circular patterns exist in the wider parts of the pore and in strongly ordered water near the constriction zone.

The ordering in OmpF stands in contrast to models of β-barrels. Although water was strongly ordered by parallel helix bundles, no significant influence of β-barrels on water structure was found (Breed et al., 1996). In the helix channels this orientation was caused by the net dipole of the helices, and was oriented such that the water dipoles compensated for the helix dipoles. The OmpF structure is much more complicated electrostatically than a simple barrel model.

A large number of water molecules are hydrogen bonded to protein atoms that are not in the immediate vicinity of the water channels. Many of these are strongly bound, judging from the average orientation over a nanosecond (Fig. 13). We did not analyze these water molecules in detail, but would like to point out that in the refined crystal structure (PDB entry 2ompf), 128 solvent atoms are included that were localized to such a degree that they are visible in the crystal structure, both inside and outside the porin.

Future work

It is reassuring that simulations on the nanosecond time scale of integral membrane helices (e.g. Shen et al., 1997) and, as we have shown here, larger integral membrane proteins, are within the capabilities of currently available computer and simulation methods. However, as in the case of larger membrane proteins, the properties of interest will often depend mostly on the internal structure of the protein; thus we have described the environment with an excessive amount of detail. Experimentally, the properties of many pores formed by aggregation of helical peptides like alamethicin (Breed et al., 1997) depend little on the lipid environment, and inclusion of lipids and corresponding large amount of water entails a large amount of unnecessary detail. As Watanabe et al. (1997) showed, the use of position restraints, even weak restraints, directly on the pore barrel can have a profound influence on the dynamics of the pore. This problem does not occur in our much more detailed system, but the computational cost is correspondingly higher.

One of the future goals should therefore be the development of a good mean field approximation to treat the bilayer with sufficient detail to not adversely influence the dynamics of the pore, without imposing "hard" restraints on any parts of the membrane protein. This approach is potentially very attractive for membrane proteins or channels that do not depend much on the specific lipid composition. Porins as used in this study make a good test system for developing such methods, because of the unambigous nature of the high-resolution crystal structure. Replacing explicit water molecules with appropriate potentials of mean force is another goal, but this approach would be too crude for the narrow parts of the pore. Whereas explicit water molecules are needed in simulations of a porin pore, they are even more necessary for simulations of ionophores.

Studying the transport properties of porins like OmpF is a second line of possible future work. Interactions with ions and polar solutes could provide a better understanding of selectivity in this type of protein, either through nonequilibrium dynamical simulations with imposed external forces or by analysis of the forces acting on particles that are restrained at various depths in the pore (Marrink and Berendsen, 1994). Nonequilibrium simulations with applied electrostatic fields would make it possible to study the local dielectric constant in the pores. This would be of interest for continuum electrostatics calculations for water-filled pores and in general further modeling of membrane channels.

CONCLUSIONS

We presented a simulation of a large integral membrane protein in a lipid bilayer with explicit lipids and solvent. During a nanosecond production run, this system remained stable, and the patterns in the secondary structure as a function of time and the root mean square fluctuations made sense, considering the topology of the protein. No con-

straints on the porins are necessary when solvent and lipids are included.

We analyzed the properties of water inside the pores and found general agreement with simpler models without lipids and with more regular pores, mainly those of Sansom and co-workers. The main differences with simpler models can be attributed to the complex combination of charged residues inside the pore and the narrow constriction zone in the middle of the pore. Much of the solvent is strongly ordered inside the pore, and the diffusion coefficients are lowered by almost an order of magnitude with respect to bulk values.

We have discussed some possible problems with equilibration and analysis methods. Future studies will be focused on nonequilibrium simulations dealing with transport and electrostatics, and on methodological work to simplify the representation of lipids and solvent far from the proteins, to maintain the benefits of the detailed treatment of the system (without the need for artificial constraints) while reducing the computational cost.

DPT was supported by the European Union under contract CT94-0124.

REFERENCES

Berendsen, H. J. C., J. R. Grigera, and T. P. Straatsma. 1987. The missing term in effective pair potentials. *J. Phys. Chem.* 91:6269–6271.

Berendsen, H. J. C., J. P. M. Postma, W. F. Gunsteren, and J. Hermans. 1981. Intermolecular Forces. Reidel, Dordrecht, the Netherlands.

Berendsen, H. J. C., J. P. M. Postma, W. F. van Gunsteren, A. DiNola, and J. R. Haak. 1984. Molecular dynamics with coupling to an external bath. *J. Chem. Phys.* 81:3684–3689.

Berendsen, H. J. C., D. van der Spoel, and R. van Drunen. 1995. GROMACS: a message-passing parallel molecular dynamics implementation. *Comp. Phys. Comm.* 91:43–56.

Berger, O., O. Edholm, and F. Jähnig. 1997. Molecular dynamics simulations of a fluid bilayer of dipalmitoylphosphatidylcholine at full hydration, constant pressure, and constant temperature. *Biophys. J.* 72: 2002–2013.

Berrier, C., A. Coulombe, C. Houssin, and A. Ghazi. 1992. Fast and slow kinetics of porin channels from *Escherichia coli* reconstituted into giant liposomes and studied by patch-clamp. *FEBS Lett.* 306:251–256.

Björkstén, J., C. M. Soares, O. Nilsson, and O. Tapia. 1994. On the stability and plastic properties of the interior 13 loop in *R. capsulatus* porin: a molecular dynamics study. *Protein Eng.* 7:487–494.

Breed, J., P. C. Biggin, I. D. Kerr, O. S. Smart, and M. S. P. Sansom. 1997. Alamethicin channels—modelling via restrained molecular dynamics simulations. *Biochim. Biophys. Acta.* 1325:235–249.

Breed, J., R. Sankararamakrishnan, I. D. Kerr, and M. S. P. Sansom. 1996. Molecular dynamics simulations of water within models of ion channels. *Biophys. J.* 70:1643–1661.

Cowan, S. W. 1993. Bacterial porins: lessons from three high-resolution structures. *Curr. Opin. Struct. Biol.* 3:501–507.

Cowan, S. W., T. Schirmer, G. Rummel, M. Steiert, R. Ghosh, R. A. Pauptit, J. N. Jansonius, and J. P. Rosenbusch. 1992. Crystal structures explain functional properties of two *E. coli* porins. *Nature.* 358:727–733.

Edholm, O., O. Berger, and F. Jähnig. 1995. Structure and fluctuations of bacteriorhodopsin in the purple membrane: a molecular dynamics study. *J. Mol. Biol.* 250:94–111.

Hille, B. 1992. Ionic Channels of Excitable Membranes, 2nd Ed. Sinauer Associates, Sunderland, MA.

Jap, B. K., and P. J. Walian. 1990. Biophysics of the structure and function of porins. *Q. Rev. Biophys.* 23:367–404.

Jeanteur, D., T. Schirmer, D. Fourel, V. Simonet, G. Rummel, C. Widmer, J. P. Rosenbusch, F. Pattus, and J.-M. Pagès. 1994. Structural and functional alterations of a colicin-resistant mutant of OmpF porin from *Escherichia coli. Proc. Natl. Acad. Sci. USA.* 91:10675–10679.

Kabsch, W., and C. Sander. 1983. Dictionary of protein secondary structure: pattern recognition of hydrogen-bonded and geometrical features. *Biopolymers.* 22:2577–2637.

Karshikoff, A., V. Spassov, S. W. Cowan, R. Ladenstein, and T. Schirmer. 1994. Electrostatic properties of two porin channels from *Escherichia coli. J. Mol. Biol.* 240:372–384.

Kraulis, P. J. 1991. MOLSCRIPT: a program to produce both detailed and schematic plots of protein structures. *J. Appl. Crystallogr.* 24:946–950.

Kreusch, A., and G. E. Schulz. 1994. Refined structure of the porin from *Rhodopseudomonas blastica*: comparison with the porin from *Rhodobacter capsulatus. J. Mol. Biol.* 243:891–905.

Marrink, S. J., and H. J. C. Berendsen. 1994. Simulation of water transport through a lipid membrane. *J. Phys. Chem.* 98:4155–4168.

Meyer, J. E. W., M. Hofnung, and G. E. Schulz. 1997. Structure of maltoporin from *Salmonella typhimurium* ligated with a nitrophenylmaltotrioside. *J. Mol. Biol.* 266:761–775.

Mouritsen, O. G., and M. Bloom. 1993. Models of lipid-protein interactions in membranes. *Annu. Rev. Biophys. Biomol. Struct.* 22:145–171.

Mouritsen, O. G., B. Dammann, H. C. Fogedby, J. H. Ipsen, C. Jeppesen, K. Jorgensen, J. Risbo, M. C. Sabra, M. M. Sperotto, and M. J. Zuckermann. 1995. The computer as a laboratory for the physical chemistry of membranes. *Biophys. Chem.* 55:55–68.

Neidhardt, F. C., J. L. Ingraham, K. B. Low, B. Magasanik, M. Schaechter, and H. E. Umbarger. 1987. *Escherichia coli* and *Salmonella typhimurium*: Cellular and Molecular Biology, Vol. 1. American Society for Microbiology, Washington, DC.

Obst, S., M. Kastowsky, and H. Bradaczek. 1997. Molecular dynamics simulations of six different fully hydrated monomeric conformers of *Escherichia coli* re-lipopolysaccharide in the presence and absence of Ca^{2+}. *Biophys. J.* 72:1031–1046.

Roux, B., and T. B. Woolf. 1996. Molecular dynamics of Pf1 coat protein in a phospholipid bilayer. *In* Biological Membranes, A Molecular Perspective from Computation and Experiment. K. M. Merz, Jr., and B. Roux, editors. Birkhäuser, Boston. 555–589.

Ryckaert, J. P., G. Ciccotti, and H. J. C. Berendsen. 1977. Numerical integration of the Cartesian equations of motion of a system with constraints: molecular dynamics of *n*-alkanes. *J. Comp. Phys.* 23: 327–331.

Sansom, M. S. P., I. D. Kerr, J. Breed, and R. Sankararamakrishnan. 1996. Water in channel-like cavities: structure and dynamics. *Biophys. J.* 70:693–702.

Sansom, M. S. P., G. R. Smith, C. Adcock, and P. C. Biggin. 1997. The dielectric properties of water within model transbilayer pores. *Biophys. J.* 73:2404–2415.

Schabert, F. A., C. Henn, and A. Engel. 1995. Native *Escherichia coli* OmpF porin surfaces probed by atomic force microscopy. *Science.* 268:92–94.

Schirmer, T., T. A. Keller, Y. F. Wang, and J. Rosenbusch. 1995. Structural basis for sugar translocation through maltoporin channels at 3.1 Å resolution. *Science.* 267:512–514.

Schulz, G. E. 1996. Porins: general to specific, native to engineered passive pores. *Curr. Opin. Struct. Biol.* 6:485–490.

Shen, L., D. Bassolino, and T. Stouch. 1997. Transmembrane helix structure, dynamics, and interactions: multi-nanosecond molecular dynamics simulations. *Biophys. J.* 73:3–21.

Smart, O. S., J. Breed, G. R. Smith, and M. S. P. Sansom. 1997. A novel method for structure-based prediction of ion channel conductance properties. *Biophys. J.* 72:1109–1127.

Soares, C. M., J. Björkstén, and O. Tapia. 1995. L3 loop-mediated mechanisms of pore closing in porin: a molecular dynamics perturbation approach. *Protein Eng.* 8:5–12.

Tieleman, D. P., and H. J. Berendsen. 1996. Molecular dynamics simulations of a fully hydrated dipalmitoylphosphatidylcholine bilayer with different macroscopic boundary conditions and parameters. *J. Chem. Phys.* 105:4871–4880.

Tieleman, D. P., J. J. L. Cascalez, and H. J. C. Berendsen. 1996. Molecular dynamics studies of lipids and proteins of the *E. coli* outer membrane: POPE and OmpF. *Prog. Biophys. Mol. Biol.* 65(Suppl.):127.

Tieleman, D. P., S. J. Marrink, and H. J. C. Berendsen. 1997. A computer perspective of membranes: molecular dynamics studies of lipid bilayer systems. *Biochim. Biophys. Acta.* 1331:235–270.

Tobias, D. J., K. Tu, and M. L. Klein. 1997. Atomic-scale molecular dynamics simulations of lipid membranes. *Curr. Opin. Colloid Interface Sci.* 2:15–26.

van der Spoel, D., A. R. van Buuren, E. Apol, P. J. Meulenhoff, D. P. Tieleman, A. L. T. M. Sijbers, R. van Drunen, and H. J. C. Berendsen. 1996a. Gromacs User Manual version 1.2. Nijenborgh 4, 9747 AG Groningen, the Netherlands (internet: http://rugmd0.chem.rug.nl/~gmx).

van der Spoel, D., A. R. van Buuren, D. P. Tieleman, and H. J. C. Berendsen. 1996b. Molecular dynamics simulations of peptides from bpti: a closer look at amide-aromatic interactions. *J. Biomol. NMR.* 8:229–238.

van Gunsteren, W. F., P. Krüger, S. R. Billeter, A. E. Mark, A. A. Eising, W. R. P. Scott, P. H. Hüneberger, and I. G. Tironi. 1996. Biomolecular Simulation: The GROMOS96 Manual and User Guide. Biomos, Groningen, and Hochschulverlag AG an der ETH Zürich, Zürich.

Warshel, A., and J. Åqvist. 1991. Electrostatic energy and macromolecular function. *Annu. Rev. Biophys. Biophys. Chem.* 20:267–298.

Watanabe, M., J. Rosenbusch, T. Schirmer, and M. Karplus. 1997. Computer simulations of the OmpF porin from the outer membrane of *Escherichia coli. Biophys. J.* 72:2094–2103.

Weiss, M. S., and G. E. Schulz. 1992. Structure of porin refined at 1.8 Å resolution. *J. Mol. Biol.* 227:493–509.

Wiese, A., G. Schroöder, K. Brandenburg, A. Hirsch, W. Welte, and U. Seydel. 1994. Influence of the lipid matrix on incorporation and function of LPS-free porin from *Paracoccus denitrificans. Biochim. Biophys. Acta.* 1190:231–242.

Woolf, T. B. 1997. Molecular dynamics of individual α-helices of bacteriorhodopsin in dimyristoyl phosphatidylcholine. I. Structure and dynamics. *Biophys. J.* 73:2476–2393.

Woolf, T. B., and B. Roux. 1996. Structure, energetics, and dynamics of lipid-protein interactions: a molecular dynamics study of the gramicidin a channel in a DMPC bilayer. *Proteins Struct. Funct. Genet.* 24:92–114.